Engineered Science

RESEARCH PAPER

View Article Online

Significantly Enhanced Ultrathin NiCo-based MOF Nanosheet Electrodes Hybrided with $Ti_3C_2T_x$ MXene for High Performance Asymmetric Supercapacitors

Yanzhong Wang,[1,2*] Yuexin Liu,[1] Chao Wang,[1,2*] Hu Liu,[3,4] Jiaoxia Zhang,[3,7] Jing Lin,[3] Jincheng Fan,[5] Tao Ding,[6] Jong E. Ryu[8] and Zhanhu Guo[3*]

In situ synthesis of NiCo based metal-organic framework (MOF) nanosheets and the exfoliation of $Ti_3C_2T_x$ into isolated nanosheets (MXene), called, NiCo-MOF/$Ti_3C_2T_x$ hybrid nanosheets, are simultaneously achieved by a facile ultrasonic method. This method can effectively avoid the oxidation and restacking of $Ti_3C_2T_x$ nanosheets, and also make them uniformly disperse on the surface of NiCo-MOF. The formed NiCo-MOF/$Ti_3C_2T_x$ hybrid nanosheets achieve a high specific capacitance of 815.2 A g^{-1} at 1 A g^{-1}. The practical asymmetric supercapacitor (ASC) is fabricated using activated carbon and NiCo-MOF/$Ti_3C_2T_x$ hybrid nanosheets. The ASC device achieves an energy density of 39.5 Wh kg^{-1} at a power density of 562.5 W kg^{-1}, and also demonstrates a suitable cycling stability with 82.3 % of capacitance retention after 10000 continuous cycles at 5 Ag^{-1}. The enhanced electrochemical property of NiCo-MOF/$Ti_3C_2T_x$ is attributed to the nanosheet-like and mesoporous structure, high electronic conductivity, and synergistic effect of hybrid electroactive components.

Keywords: MOF; MXene; Nanosheets; Pseudocapacitor; Ti_3AlC_2; Asymmetrical supercapacitors

Received 4 November 2019, **Accepted** 6 January 2020

DOI: 10.30919/es8d903

1. Introduction

The depletion of fossil fuel, serious environmental pollution and global warming have stimulated extensive explorations of renewable clean energy (solar, wind, and hydrogen energies *et al.*). Nevertheless, the intermittent nature of renewable energies requires efficient energy storage units to supply continuous and stable energy, including batteries, fuel cells, and supercapacitors. In these various energy storage devices, supercapacitors have attracted tremendous attention owing to their fast charging and discharging, high power densities and long-term stability. [1] In the light of the charge-storage mechanism, supercapacitors generally contain two categories: (1) electric double layer capacitors (EDLCs, based on the charges absorbed at the interface of electrode and electrolyte) possess remarkable cycling stability and power density, but exhibit low specific capacitance; (2) pseudocapacitors (involving fast reversible surface redox faradaic reactions) offer relatively high specific capacitances. [2] In general, the structures and properties of electrode materials significantly influence the electrochemical performance of supercapacitors such as the specific capacitance, rate capability, and cycle life.[3] Currently, carbon-based materials,[4] transition metal oxides,[5] conducting polymers, [6] and their composites, [7] have been investigated for supercapacitor electrodes. However, these electrode materials have demonstrated their shortcomings for applications in supercapacitors such as low specific capacitances for carbon-based materials, limited electronic conductivity for transition metal oxides, and short cycle life for

[1]*School of Materials Science and Engineering, North University of China, Taiyuan 030051, China*
[2]*Advanced energy materials and system institute, North University of China, Taiyuan 030051, China*
[3]*Integrated Composites Laboratory (ICL), Department of Chemical & Biomolecular Engineering, University of Tennessee, Knoxville, TN 37966, USA*
[4]*Key Laboratory of Materials Processing and Mold (Zhengzhou University), Ministry of Education, National Engineering Research Center for Advanced Polymer Processing Technology, Zhengzhou University, Zhengzhou, China*
[5]*College of Materials Science and Engineering, Changsha University of Science and Technology, Changsha 410114, China*
[6]*College of Chemistry and Chemical Engineering, Henan University, Kaifeng 475004, China*
[7]*School of Materials Science and Engineering, Jiangsu University of Science and Technology, Zhenjiang 212003, China*
[8]*Department of Mechanical and Aerospace Engineering, North Carolina State University, Raleigh, NC 27695, USA*
***E-mail:** wyzletter@nuc.edu.cn(Y. Z. Wang); wangchao_nuc@126.com (C. Wang) ; zguo10@utk.edu (Z. Guo)*

conducting polymers.[8] Therefore, many studies have focused on developing new electrode materials with a large specific surface area and high electronic conductivity.

MOFs are formed by strong coordination bonds between metal ions and organic ligands, and their structures and properties can be facilely regulated by choosing different metal centers and ligands.[9, 10] These merits make them have extensive applications in catalysis, gas storage and separation, sensors, bio-medicine, and energy storage and conversion. [11-13] Especially, the unique structure and properties of MOFs are very suitable for high-performance supercapacitor electrode materials such as the extremely large specific surface area, easily adjustable pore size, and abundant pseudocapacitive redox centers. [10] The MOF-based supercapacitor electrode materials mainly include two categories. One is that MOFs are employed as an excellent precursor to prepare porous carbons, [14] various transition metal compounds (oxides, selenides, sulfides, and phosphides *et al*.),[15-19] and their composites under different preparation conditions. [20] Although these materials generally exhibit outstanding electrochemical performances, the prolonged and multi-step processes inevitably increase the production cost. Furthermore, the thermal or chemical treatments would inevitably destroy the porous structure of MOFs, and thus reducing the accessible surface area and the number of electroactive sites. [21] The other is that MOFs are directly employed as electrode materials for high-performance supercapacitors. However, the limited electronic conductivity of MOFs becomes a big obstacle in the practical application of supercapacitors.[22]

In order to circumvent the issue, one way is to develop highly conductive MOFs by adjusting the structure and components. For instance, Jiao's and Wei's groups reported the existence of conductive network in the layer-structured Co-MOF and Ni-MOF that can make electrons transfer rapidly in the MOF framework and significantly improve their electronic conductivity, and thus resulting in the excellent capacitive performance. [23-25] The other strategy is that the conductive substrates such as graphene,[21, 26-28] CNTs,[29, 30] polyaniline[31, 32] and polypyrrole[33] are employed to boost the electronic conductivity of MOFs. For example, Banerjee *et al*. synthesized Ni-MOF/rGO composites via a hydrothermal method that exhibited a specific capacitance of 758 F g^{-1}, and the assembled device delivered an energy density of 37.8 Wh kg^{-1}.[34] Wen *et al*. prepared Ni-MOF/CNT composites with high electronic conductivity, indicating a maximum specific capacitance of 1765 F g^{-1}.[29] Shao *et al.* in situ form polyaniline chains in the pores of UiO-66 to enhance its electronic conductivity, indicating the remarkable electrochemical performance. [31] However, the above conductive substrates only play an important role in improving the electronic conductivity, but have little contribution to the specific capacitance of composites. Moreover, the preparation process of these conductive substrates is complex and costly.

MXenes, as novel 2D transition metal carbides and nitrides, have aroused extraordinary interest in supercapacitors owing to their metallic conductivity, large specific surface area, and high packing density.[35, 36] Among these different MXenes, $Ti_3C_2T_x$ (T stands for a surface terminating functionality including －O, －OH, and －F), has been widely investigated. For instance, Gogotsi *et al*. first prepared the accordion-like $Ti_3C_2T_x$ by selectively etching Al elements of Ti_3AlC_2 using HF, which gave a specific capacitance of 130 F g^{-1}.[37] By virtue of the high electronic conductivity and 2D structure of $Ti_3C_2T_x$ nanosheets, they have been widely employed as a conductive agent or template to boost the electronic conductivity of carbon nanomaterials,[38] metal oxides,[39] conducting polymers,[40] and MOFs [41, 42] for enhancing their electrochemical properties. In the preparation of the above-mentioned composite materials, the isolated $Ti_3C_2T_x$ nanosheets were first prepared by an ultrasonification under Ar atmosphere, and then compounded with other materials, which easily results in the oxidation and restacking of $Ti_3C_2T_x$ nanosheets, [43] and thus losing the advantages of $Ti_3C_2T_x$.

Herein, the in-situ synthesis of NiCo-MOF nanosheets and the exfoliation of $Ti_3C_2T_x$ were simultaneously achieved by an ultrasonic method, which can effectively avoid the oxidation and restacking of $Ti_3C_2T_x$ nanosheets during the preparation process, and also make isolated $Ti_3C_2T_x$ nanosheets uniformly distribute on the surface of NiCo-MOF. In NiCo-MOF/$Ti_3C_2T_x$ hybrid nanosheets, $Ti_3C_2T_x$ can act as a conductive agent to enhance the electronic conductivity as well as a spacer to effectively prevent the agglomeration of NiCo-MOF. It is well known that 2D nanosheets possess high specific surface area, a large number of electroactive sites, and rapid transfer pathway for ion and electron, which would result in the excellent capacitive performance. Accordingly, the rationally designed NiCo-MOF/$Ti_3C_2T_x$ hybrid nanosheets achieved a high specific capacitance of 815.2 F g^{-1} at 1 A g^{-1}. Moreover, the fabricated NiCo-MOF/$Ti_3C_2T_x$//AC asymmetric supercapacitors exhibited a high energy density of 39.5 Wh kg^{-1} with the power density of 562.5 W kg^{-1} and excellent cycling performance (82.3% of capacitance retention after 10000 cycles).

2 Experimental

2.1 Chemicals

$NiCl_2 \cdot 6H_2O$, $CoCl_2 \cdot 6H_2O$, LiF, p-phthalic acid (PTA, 98%), dimethylformamide (DMF, 99.8%), hydrochloric acid (HCl, 36%), and trimethylamine (TEA, 98%) were purchased from Aladdin, and used without any purification. Ti_3AlC_2 powders (~99.998%) were purchased from Foreshman.

2.2 Synthesis of $Ti_3C_2T_x$

Typically, 2 g of LiF was slowly dissolved into 40 mL HCl

(9 M) under stirring, and then 2 g of Ti_3AlC_2 powders were slowly added into the above solution. The mixture was stirred at 40 °C for 24 h. After etching, the mixture was washed five times by centrifugation with deionized water and absolute alcohol until the pH reached 6. The resultant powders were dried at 60 °C for overnight.

2.3 Synthesis of NiCo-MOF/$Ti_3C_2T_x$ Hybrid Nanosheets

NiCo-MOF nanosheets was prepared as the previous report with some modifications.[44, 45] In a typical synthesis of NiCo-MOF/ $Ti_3C_2T_x$ hybrids, 5 mg $Ti_3C_2T_x$ was added into the DMF solution containing Co^{2+}, Ni^{2+}, PTA and TEA. Subsequently, the mixture was ultrasonicated for 8 h under Ar flowing. The resultant powers were washed by a centrifugation with ethanol for 3 times, and dried at 60 °C for 12 h. The as-prepared NiCo-MOF/$Ti_3C_2T_x$ hybrid nanosheets were denoted as NiCo-MOF/Ti-5. For comparison, NiCo-MOF/Ti-*x* (x=2.5 and 10 mg) and NiCo-MOF were synthesized under the same experimental condition.

The detailed characterizations and electrochemical measurements can be referred to electrical supporting information.

3 Results and Discussion

3.1 Structures and Functionality Characterization of the MOF-MXene Hybrid Nanosheets

The synthetic process of NiCo-MOF/$Ti_3C_2T_x$ hybrid nanosheets is shown in Fig. 1. Typically, $Ti_3C_2T_x$ was synthesized by etching Al layers from Ti_3AlC_2 powders with LiF and HCl solution. The negatively charged groups (*e.g.* -O, -OH, and -F) on the surface of $Ti_3C_2T_x$ could absorb Ni^{2+} and Co^{2+} ions due to the electrostatic force that coordinate with PTA ligand and in situ form NiCo-MOF nanosheets under ultrasonication. Herein, the ultrasonication can not only exfoliate the accordion-like $Ti_3C_2T_x$ into isolated nanosheets, but also in situ synthesize NiCo-MOF nanosheets, resulting in the tight contact of NiCo-MOF and $Ti_3C_2T_x$ nanosheets. The intimate contact structure is convenient for the electron transfer from NiCo-MOF to $Ti_3C_2T_x$, thus enhancing the electronic conductivity of NiCo-MOF/$Ti_3C_2T_x$ hybrid nanosheets. Compared with the previously reported method to synthesize MOF/$Ti_3C_2T_x$ composites,[44, 46] this method is facile and cost-effective to prepare NiCo-MOF/$Ti_3C_2T_x$ hybrid nanosheets.

The microstructures of as-prepared samples were characterized by SEM and TEM. Fig. S1a and b show that the large-area exfoliated $Ti_3C_2T_x$ exhibits thin and crumpled nanosheets, and no accordion-like structures were observed, indicating the complete exfoliation of $Ti_3C_2T_x$.[47] In the high resolution TEM (HRTEM) image of $Ti_3C_2T_x$ nanosheets (Fig. S1c), the edge of a typical nanosheet demonstrates a few layers thick with the average interlayer spacing of 1.2 nm. Fig. 2a and b show that the NiCo-MOF/Ti-5 hybrid nanosheets display curved nanosheets, and their random distribution effectively prevents the restacking of NiCo-MOF/Ti-5 hybrid nanosheets. In addition, the hybrid nanosheets have a lateral length of several micrometers with nanoscale thickness. In comparison, without the addition of $Ti_3C_2T_x$, the NiCo-MOF nanosheets prepared by the same experimental process were aggregated into the bulk materials (Fig. S2a). As shown in Fig. S2b and c, the agglomeration of hybrid nanosheets obviously decreases with $Ti_3C_2T_x$ contents.

The microstructures of NiCo-MOF/Ti-5 hybrid nanosheets were further examined by TEM observations as shown in Fig. 2c. It also confirms the sheet-like morphology of NiCo-MOF/Ti-5 hybrid composites, which were stacked by several layers with different lateral lengths. Fig. 2c and d shows that $Ti_3C_2T_x$ nanosheets with a length of 50~100 nm were evenly embedded on surfaces of NiCo-MOF nanosheets. The size of $Ti_3C_2T_x$ nanosheets in NiCo-MOF/Ti-5 is much smaller than that of pristine $Ti_3C_2T_x$ nanosheets (Fig. S1), which is assigned to the long-term ultrasonication. The HRTEM image of NiCo-MOF/Ti-5 hybrid nanosheets reveals the existence of nanoclusters with a dimeter of 3~5 nm on the NiCo-MOF marked by the red circles, indicating the lattice fringes derived from nickel-cobalt oxide in the inset (Fig. 2e), which is similar to the previous report.[25, 48] Meanwhile, Fig. 2f indicates the visible lattice fringes with a spacing of about 0.24 nm, which corresponds to the (103) lattice plane of $Ti_3C_2T_x$.[49] The dark-field scanning TEM (STEM) image with the associated EDX elemental mapping exhibit the existence of Ti, Co, Ni, C, and O elements, further confirming the successful hybridization of $Ti_3C_2T_x$ with NiCo-MOF (Fig. 2 g-m). The thickness of NiCo-MOF/Ti-5 hybrid nanosheets was examined by atomic force microscopy (AFM). By drawing a line profile across the stacked NiCo-

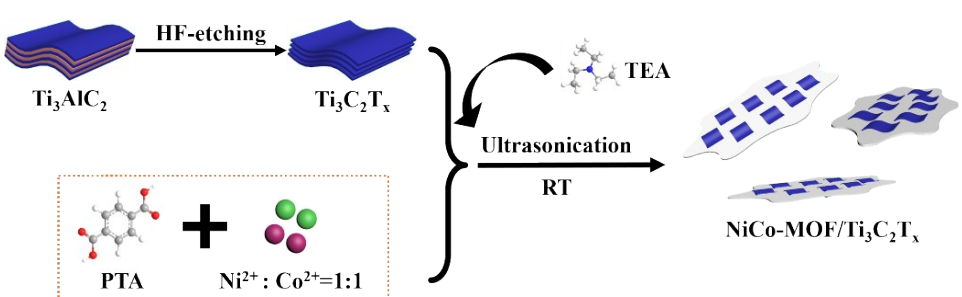

Fig. 1 Scheme of the synthesis of NiCo-MOF/$Ti_3C_2T_x$.

MOF/Ti-5 hybrid nanosheets (Fig. S3), the thickness of hybrid nanosheets was found to be 2.7 ~ 5 nm, which is close to the value of the previous report.[35]

The crystal structures of Ti_3AlC_2 and exfoliated $Ti_3C_2T_x$ nanosheets were examined by XRD measurements. Fig. S4 shows that the weak peaks at 19 and 39° of $Ti_3C_2T_x$ are assigned to the (004) and (104) planes of Ti_3AlC_2, respectively, suggesting the incomplete remove of the Al layer by etching. In addition, $Ti_3C_2T_x$ exhibited an enlarged interlayer spacing evidenced by the smaller 2θ of (002) peak compared with Ti_3AlC_2 due to the removal of Al layers.[50] Fig. 3a shows the XRD patterns of as-synthesized NiCo-MOF/$Ti_3C_2T_x$ hybrid nanosheets. NiCo-MOF exhibits the similar XRD pattern with Co-MOF (JCPDS 985792, C2/m).[51] Here, Co and Ni ions are octahedrally coordinated to hydroxyls, and these pseudo octahedrals are connected to form layered structure. The layers are bridged by the terephthalate groups to form the three-dimensional layered structure.[25] These peaks were also presented in the XRD patterns of NiCo-MOF/$Ti_3C_2T_x$ hybrid nanosheets. Nevertheless, the peak intensities of NiCo-MOF/$Ti_3C_2T_x$ hybrid nanosheets gradually decrease with increasing the $Ti_3C_2T_x$ content, suggesting that the $Ti_3C_2T_x$ nanosheets suppress the degree of crystalline of NiCo-MOF. No peaks corresponding to $Ti_3C_2T_x$ in the NiCo-MOF/$Ti_3C_2T_x$ were observed, indicating that the accordion-like $Ti_3C_2T_X$ was delaminated into few-layer nanosheets by the ultrasonication.[52]

The functional groups on the surface of as-prepared samples were examined by FT-IR. Fig. S5 a shows that the peaks of $Ti_3C_2T_x$ at 3441, 1634, 1448, 1037, and 617 cm^{-1} are attributed to the stretching vibrations of – OH, C=O, O – H, C – F and Ti – O bonds.[53] As shown in Fig. 3b and Fig. S5b, NiCo-MOF/$Ti_3C_2T_x$ hybrid nanosheets exhibited identical stretching vibrations to NiCo-MOF, and very weak peaks at 1634 and 617 cm^{-1} correspond to the C=O and Ti-O in the $Ti_3C_2T_x$, respectively. The distinct peak at 3441 cm^{-1} belongs to the -OH stretching vibration,[54] and two strong peaks at 1593 and 1392 cm^{-1} are assigned to the v_{as} (-COO) and v_s (-COO) of terephthalate anions, respectively.[25] The peaks at 818 and 770 cm^{-1} account for the stretching bands of para-aromatic C-H. The results agree well with the previous characterizations of $[Co_2(OH)_2C_8H_4O_4]$.[25, 55]

The pore texture and specific surface area of samples

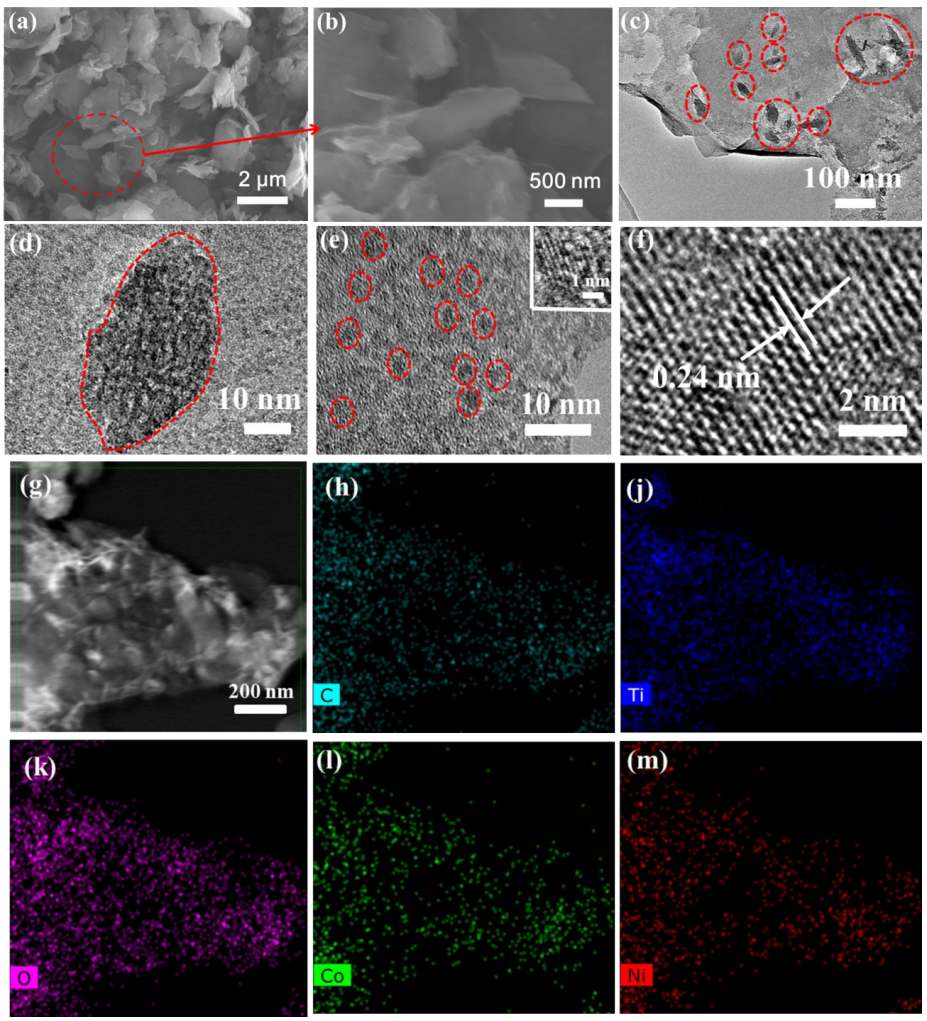

Fig. 2 (a) and (b) SEM images, (c) TEM image, (d-f) HRTEM images, (g-m) STEM images and EDX mapping of NiCo-MOF/Ti-5.

were measured by N_2 sorption isotherms as shown in Fig. 3c and d and Fig. S6. Fig. 3c shows that the isotherm curves of all samples exhibit type IV with a H_3 hysteresis loop, revealing the existence of mesopores.[14] Fig. 3d shows the pore sizes of NiCo-MOF and NiCo-MOF/$Ti_3C_2T_x$ mostly located in the range from 2 to 6 nm, which further confirmed their mesoporous structures. The specific surface areas of samples are displayed in Table S1. The pristine NiCo-MOF exhibited larger specific surface area than that of NiCo-MOF/$Ti_3C_2T_x$ hybrid nanosheets owing to the low specific surface area of $Ti_3C_2T_x$. However, the specific surface area of NiCo-MOF gradually increased with $Ti_3C_2T_x$ contents, such as the 13.54 m^2 g^{-1} for NiCo-MOF/Ti-2.5, 22.56 m^2 g^{-1} for NiCo-MOF/Ti-5, and 25.57 m^2 g^{-1} for NiCo-MOF/Ti-10, respectively. This indicates that that $Ti_3C_2T_x$ can prevent the agglomeration of NiCo-MOF, which is also confirmed by the SEM images in Fig. 2 and Fig. S2.

The surface electronic state and composition of NiCo-MOF/Ti-5 hybrid nanosheets were characterized by XPS. The XPS survey spectrum (Fig. 4a) indicates the presence of C, Ni, Co, O, and Ti elements, which was in agreement with the results of EDX. The element content (Table S2) shows that the atomic ratio of Co and Ni ions is about 0.8, which approximates the atomic ratio of Co and Ni salts. Fig. 4b demonstrates the high-resolution Co 2p spectrum of NiCo-MOF/$Ti_3C_2T_x$, illustrating two major peaks located at 797. 4 and 781.4 eV that correspond to Co $2p_{1/2}$ and Co $2p_{3/2}$ of Co^{2+} in NiCo-MOF,[56] and two shake-up satellite at 803.2 and 785.9 eV. Regarding the Ni 2p spectra (Fig. 4c), the fitting peaks at 873.8 and 856.3 eV with a spin-energy separation of 17.5 eV and satellite peaks at 880.1 and 861.5 eV correspond to the Ni $2p_{1/2}$ and Ni $2p_{3/2}$ spin-orbits, respectively, suggesting the Ni^{2+} oxidation state in the NiCo-MOF.[57] The high-resolution C 1s spectrum (Fig. 4d) presented four peaks at 288.5, 287.9, 285.3 and 284.5 eV, which can be assigned to C=C, C-O, C=O, and O – C=O bonds, respectively.[58] In the O 1s spectrum (Fig. 4e), two major peaks at 532.4 and 531.4 eV are attributed to the metal oxygen bond (M – O – M) and hydroxyl oxygen (– OH).[57] The Ti 2p spectrum (Fig. 4f) shows two doublets corresponding to Ti $2p_{3/2}$ and Ti $2p_{1/2}$. Two peaks located at 457.7 and 463.5 eV are attributed to Ti-C, and the other two peaks at 458.6 and 464.1 eV are attributed to Ti-O, which match well with the reported pure MXene.[59]

3.2. Electrochemical Performance Evaluaton the MOF-MXene Hybrid Elecrode

The electrochemical properties of samples were examined by CV, GCD and EIS measurements in a three-electrode system in 2 M KOH electrolyte. Fig. 5a shows the CV curves of NiCo-MOF and NiCo-MOF/$Ti_3C_2T_x$ electrodes at a scan rate of 10 mV s^{-1}. Obviously, a pair of well-defined redox peaks was observed for all the CV curves between 0.2 and 0.4 V, indicating the pseudocapacitive nature.[60] In addition, NiCo-MOF/Ti-5 exhibits the larger CV area than that of other samples, demonstrating that NiCo-MOF/Ti-5 can deliver the highest specific capacitance comparing with other samples. Fig. 5b shows the GCD curves at 1 A g^{-1}. The obvious discharge potential platform further indicates the pseudocapacitance characteristics. Moreover, the discharge time of NiCo-MOF/Ti-5 electrode is much longer than that of

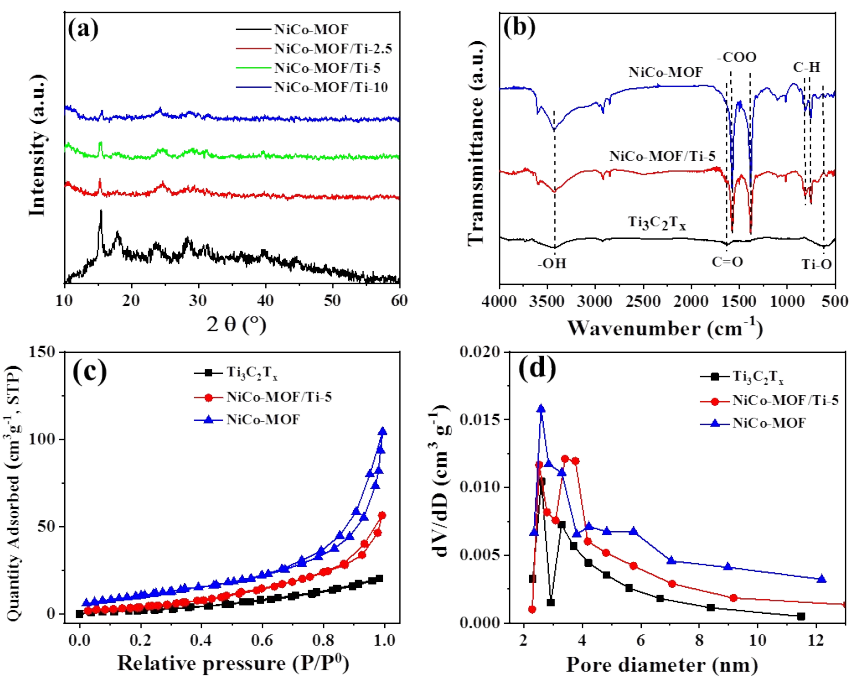

Fig. 3 (a) XRD patterns of NiCo-MOF/$Ti_3C_2T_x$, (b) FT-IR spectra, (c) N_2 adsorption-desorption isotherms, and (d) the pore size distribution of $Ti_3C_2T_x$, NiCo-MOF and NiCo-MOF/Ti-5.

other electrodes, demonstrating a higher specific capacitance, which agrees with the results of CV curves in Fig. 5a. Accordingly, the electrochemical properties of NiCo-MOF/Ti-5 and other samples were further tested by CV and GCD measurements. The CV curves were tested at scan rates of 5 - 100 mV s^{-1} in Fig. 5c and Fig. S7. The redox peaks are still observed even at the scan rate of 100 mV s^{-1}, indicating excellent rate performance.[61] In addition, with increasing the scan rates, the anodic peak moves gradually toward more positive potential, while the cathodic peak moves toward more negative potentials, respectively. This shift in redox peaks is generally assigned to improving the polarization of charge transfer in the electrode material.[8, 62] The GCD curves were measured at different current densities. Fig. 5d and Fig. S7 show that all the GCD curves exhibit similar shapes with the distinct potential plateau regions, indicating similar pseudocapacitive behavior. In addition, the approximately symmetric GCD curves display the excellent reversibility of the faradaic redox reactions and high columbic efficiency.[61]

The calculated specific capacitances of all samples based on GCD curves are shown in Fig. 5e. It can be seen that the NiCo-MOF/Ti-5 electrode exhibits the maximum specific capacitance, and the specific capacitances reach up to 835.8, 815.2, 761.4, 726.3, 684.5, 643.7, and 571.2 at 0.5, 1, 3, 5, 7, 10, and 20 A g^{-1}, respectively. Moreover, NiCo-MOF/Ti-5 also indicates the good rate capability (the capacitance retains 64.6% at 0.5-20 A g^{-1}). Compared with the recently reported $Ti_3C_2T_x$ based electrode materials such as GO-$Ti_3C_2T_x$@Polyaniline,[63] and MnO_2@ $Ti_3C_2T_x$,[64] the NiCo-MOF/Ti-5 electrode archives superior special capacitance, which is assigned to 2D mesoporous structure and excellent electronic conductivity. The cycling stability of NiCo-MOF/Ti-5 was investigated at 5 A g^{-1} over continuous 5000 cycles of charging and discharging (Fig. S8). The capacitance retention was found to be 93.4 % of the initial capacitance after 5000 cycles.

EIS was carried out to further investigate the electron transfer and ions diffusion at the electrode/electrolyte interface, and Nyquist plots are shown in Fig. 5f. The semicircle at the

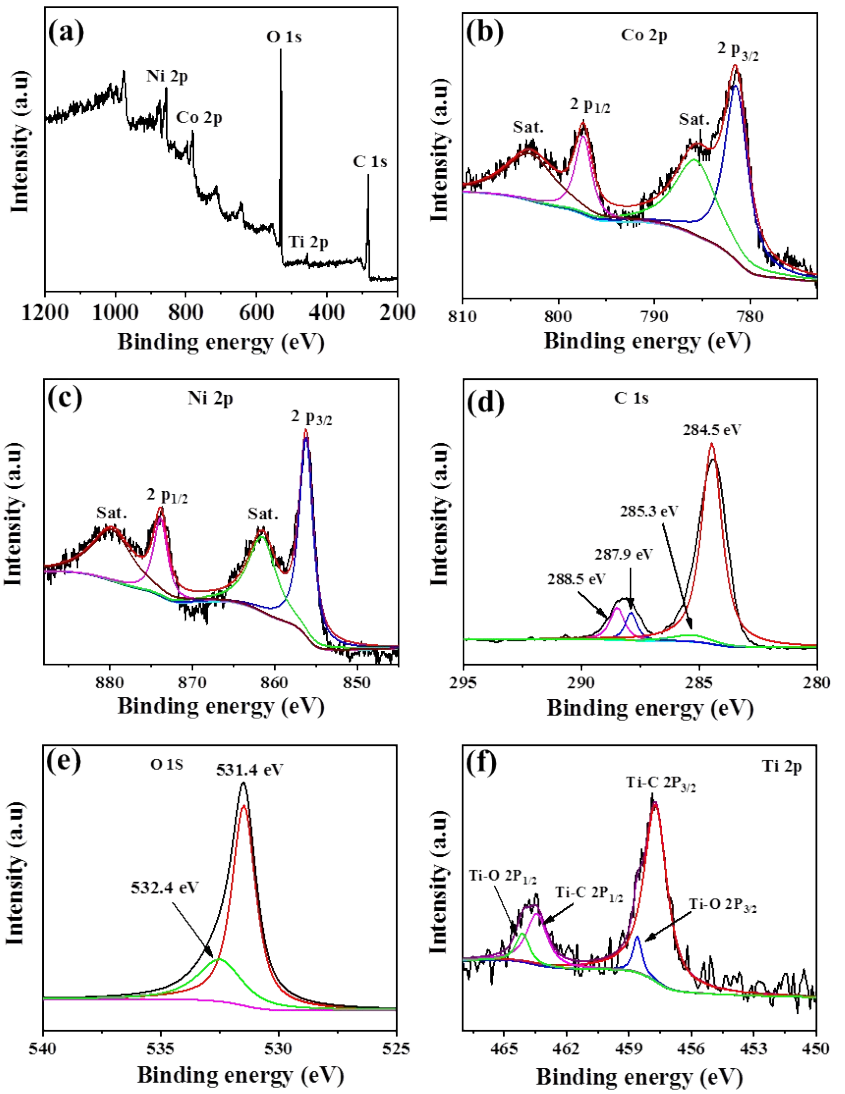

Fig. 4 (a) XPS survey spectrum of NiCo-MOF/Ti-5, and the high-resolution XPS spectra of (b) Co 2p, (c) Ni 2p, (d) C 1s, (e) O 1s, and (f) Ti 2p.

high frequency is attributed to the charge-transfer resistance (R_{ct}), and the intercept at the real axis indicates the equivalent series resistance (R_s).[57] Obviously, the R_s of samples declines with the increase of $Ti_3C_2T_x$ content, such as the values of R_s are 0.54, 0.42, 0.29, and 0.16 Ω for the pristine NiCo-MOF, NiCo-MOF/Ti-2.5, NiCo-MOF/Ti-5, and NiCo-MOF/Ti-10, respectively. The low R_{ct} of all samples is attributed to the nanosheet-like and mesoporous structure that provide rapid transfer pathway for ion and electron.

3.3 Evaluation of Asymmetric Supercapacitors

An asymmetric supercapacitor (ASC) was fabricated by using NiCo-MOF/Ti-5 as the positive electrode and activated carbon (AC) as the negative electrode, and polypropylene film as a separator. The schematic diagram of the ASC device is illustrated in Fig. 6a, and CV and GCD measurements of the AC electrode were carried out in a three-electrode system (Fig. S9). Based on the charge balance of positive and negative electrodes, the mass ratio of NiCo-MOF/Ti-5 and AC was calculated to be 0.49 according to the Equation S2. Herein, the total mass loading of the device was about 9.1 mg cm^{-2} (NiCo-MOF was ~3 mg cm^{-2} and ACs was ~6.1 mg cm^{-2}). Fig. 6b reveals that the operating potential window of AC can be in the range from -1.0 to 0 V, and NiCo-MOF/Ti-5 from 0 to 0.5 V. Thus, the operating voltage of the assembled asymmetric supercapacitor can be extended to 1.5 V, which was further confirmed by the CV curves of the ASC device at a scan rate of 30 mV s^{-1} in the Fig. 6c. No polarization of ASC device was observed in a voltage of 0 to 1.5 V. As shown in Fig. 6d, the CV curves of the ASC device at the scan rates from 5 to 50 mV s^{-1} indicate the typical capacitive behavior and good rate performance. The GCD curves (Fig. 6e) show the symmetric

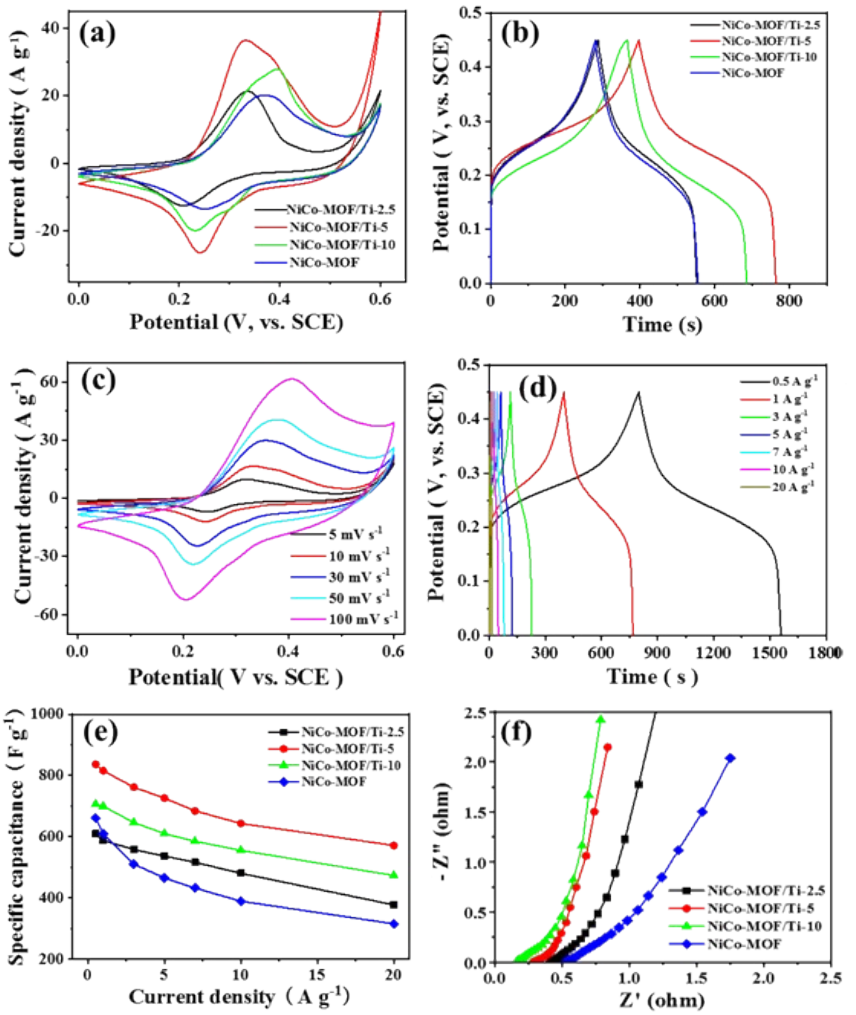

Fig. 5 (a) CV curves of NiCo-MOF and NiCo-MOF/$Ti_3C_2T_x$ electrodes at a scan rate of 5 mV s^{-1}, (b) GCD curves of NiCo-MOF and NiCo-MOF/$Ti_3C_2T_x$ electrodes at a current density of 1 A g^{-1}, (c) CV curves of NiCo-MOF/Ti-5 electrode at different scan rates, (d) GCD curves for NiCo-MOF/Ti-5 electrode at different current densities, (e) the specific capacitance at different current densities, and (f) Nyquist plots of NiCo-MOF and NiCo-MOF/$Ti_3C_2T_x$ electrodes (inset: magnified region).

charging and discharging curves without any distinct voltage drop at 0.5-20 A g^{-1}, revealing the excellent rate capability. The specific capacitances of the ASC device are 126.38, 115.68, 92.04, 76.5, 62.5, 53.6, and 40.7 F g^{-1} at 0.5, 1, 3, 5, 7, 10, and 20 A g^{-1}, respectively (Fig. 6f). The electrochemical impedance spectra of the device were tested in the frequency of 0.01 – 10^5 Hz, and the Nyquist plot is shown in the Fig. S10. The equivalent series resistance (R_s) is 1.12 Ω, and the charge-transfer resistance (R_{ct}) of 3.16 Ω. The steep slope of the Warburg line indicates the low diffusion resistance of

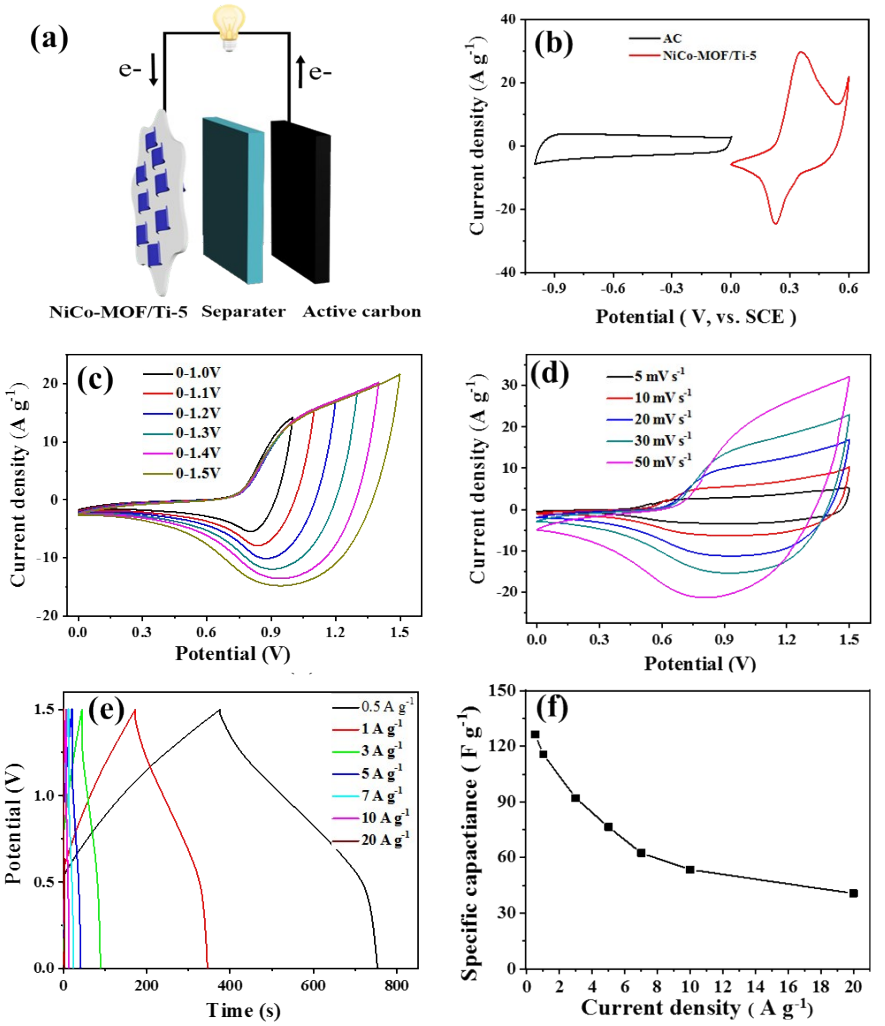

Fig. 6 (a) Schematic of assembled asymmetric supercapacitor, (b) CV curves of NiCo-MOF/Ti-5 and ACs at a scan rate of 30 mV s^{-1}; (c) CV curves at a scan rate of 30 mV s^{-1} in different potential windows, (d) CV curves at different scan rates, (e) GCD curves at different current densities, (f) the relationship of the specific capacitance with current densities of the ASC device.

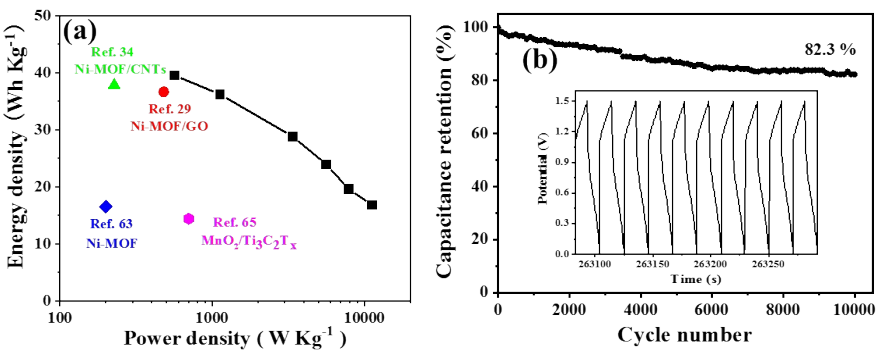

Fig. 7 (a) Ragone plot, (b) the cyclic stability of NiCo-MOF/Ti-5//AC at a current density of 5 A g^{-1} for 10,000 cycles.

electrolyte ions.

The energy density and power density are key parameters for evaluating the practical performance of supercapacitors, and they can be calculated from the charge/discharge curves according to Equation S3 and S4. The relationship between energy density and power density of NiCo-MOF/Ti-5//ACs device is presented via the Ragone plot in Fig. 7a. The device achieves a power density of up to 22.5 kW kg^{-1} and the maximum energy density of 39.5 Wh kg^{-1}, which are superior to those of previously reported asymmetric supercapacitor systems, such as Ni-MOF/CNTs//rGO/g-C_3N_4,[29] Ni-MOF/rGO//AC,[34] Ni-MOF//AC,[65] and $MnO_2/Ti_3C_2T_x$// $MnO_2/Ti_3C_2T_x$.[64]

The cycle stability of our device was tested by repeatedly charging and discharging for 10000 cycles at 5 A g^{-1} as presented in Fig. 7b. The NiCo-MOF/Ti-5//AC device have retained 82.3 % of its specific capacitance after 10000 cycles, and the insert of Fig. 7b exhibits that last 10 charge/discharge cycles reveal only minor changes, demonstrating the excellent cycling stability. To demonstrate the real application of our device, two assembled NiCo-MOF/Ti-5//AC asymmetric supercapacitor devices were connected in series, and they can light the red light emitting diode (LED) for 30 min (Fig. S11), indicating the potential practical application of the device.

The above results show that the as-synthesized NiCo-MOF/Ti-5 hybrid nanosheets possess excellent capacitive performances, which can be assigned to the following reasons: (1) the ultrathin sheet-like and mesoporous structure can not only offer a number of electroactive sites but also shorten the transfer pathway for electron and ion; (2) the uniform dispersion of $Ti_3C_2T_x$ on the surface of ultrathin NiCo-MOF nanosheets makes them tightly contact, and thereby effectively enhancing the electron transfer at the interface between NiCo-MOF and $Ti_3C_2T_x$ nanosheets; (3) $Ti_3C_2T_x$ nanosheets can effectively prevent the agglomeration of NiCo-MOF as a spacer, and thus resulting in more exposed active sites.

4. Conclusions

Herein, the in situ synthesis of NiCo-MOF and the exfoliation of $Ti_3C_2T_x$ were simultaneously achieved by an ultrasonic method, which can effectively avoid the oxidation and restacking of $Ti_3C_2T_x$ nanosheets during the preparation process. The isolated $Ti_3C_2T_x$ nanosheets were evenly distributed on the surface of NiCo-MOF nanosheets, which can boost the electronic conductivity as well as effectively hinder the agglomeration of NiCo-MOF nanosheets. The unique structure makes NiCo-MOF/$Ti_3C_2T_x$ hybrid nanosheets exhibit a high specific capacitance of 815.2 F g^{-1} at 1 A g^{-1}, remarkable rate capability and cycle life. Furthermore, the NiCo-MOF/Ti-5//AC ASC archives the maximum energy density of 39.5 Wh kg^{-1} at a power density of 562.5 W kg^{-1}, and still remains 12.7 Wh kg^{-1} at the maximum power density of 22.5 kW kg^{-1}. The impressive electrochemical performance shows the great potential applications in the high-performance supercapacitors.

Conflict of Interest

There are no conflicts to declare.

Acknowledgments

The work was financially supported by Shanxi Province Science Foundation (No. 201801D121284), and Program for the Innovative Talents of Higher Education Institutions of Shanxi.

References

1. Y. Wang, Y. Song and Y. Xia, *Chem. Soc. Rev.*, 2016, **45**, 5925-5950.
2. W. Raza, F. Ali, N. Raza, Y. Luo, K. H. Kim, J. Yang, S. Kumar, A. Mehmood and E. E. Kwon, *Nano Energy*, 2018, **52**, 441-473.
3. Y. Tan, Y. Liu, L. Kong, L. Kang and F. Ran, *J. Power Sources*, 2017, **363**, 1-8.
4. H. Jiang, P. S. Lee and C. Li, *Energy Environ. Sci*., 2013, 6, 41-53.
5. J. Jiang, Y. Li, J. Liu, X. Huang, C. Yuan and X. W. Lou, *Adv. Mater.*, 2012, **24**, 5166-5180.
6. G. A. Snook, P. Kao and A. S. Best, *J. Power Sources*, 2011, **196**, 1-12.
7. M. Zhi, C. Xiang, J. Li, M. Li and N. Wu, *Nanoscale*, 2013, **5**, 72-88.
8. S. G. Mohamed, I. Hussain and J. J. Shim, *Nanoscale*, 2018, **10**, 6620-6628.
9. J. Liu, D. Zhu, C. Guo, A. Vasileff and S. Z. Qiao, *Adv. Energy Mater.*, 2017, **7**, 1700518.
10. S. Zheng, X. Li, B. Yan, Q. Hu, Y. Xu, X. Xiao, H. Xue and H. Pang, *Adv. Energy Mater.*, 2017, **7**, 1602733.
11. S. Wang, Q. Wang, X. Feng, B. Wang and L. Yang, *Adv. Mater.*, 2017, **29**, 1701898.
12. Z. Kang, L. Fan and D. Sun, *J. Mater. Chem. A*, 2017, **5**, 10073-10091.
13. A. Dhakshinamoorthy, Z. Li and H. Garcia, *Chem. Soc. Rev.*, 2018, **47**, 8134-8172.
14. S. Zhong, C. Zhan and D. Cao, *Carbon*, 2015, **85**, 51-59.
15. M. Jin, S. Y. Lu, L. Ma, M. Y. Gan, Y. Lei, X. L. Zhang, G. Fu, P. S. Yang and M. F. Yan, *J. Power Sources*, 2017, **341**, 294-301.
16. Y. Zhang, A. Pan, Y. Wang, X. Cao, Z. Zhou, T. Zhu, S. Liang and G. Cao, *Energy Storage Mater.*, 2017, **8**, 28-34.
17. Y. Xu, S. Hou, G. Yang, X. Wang, T. Lu and L. Pan, *Electrochim. Acta*, 2018, **285**, 192-201.
18. Z. Jiang, Z. Li, Z. Qin, H. Sun, X. Jiao and D. Chen, *Nanoscale*, 2013, **5**, 11770-11775.
19. B. Han, G. Cheng, E. Zhang, L. Zhang and X. Wang, *Electrochim. Acta*, 2018, **263**, 391-399.
20. A. Jayakumar, R. P. Antony, R. Wang and J. M. Lee, *Small,* 2017, **13**, 1603102.
21. M. S. Rahmanifar, H. Hesari, A. Noori, M. Y. Masoomi, A. Morsali and M. F. Mousavi, *Electrochim. Acta*, 2018, **275**, 76-86.
22. L. Wang, Y. Han, X. Feng, J. Zhou, P. Qi and B. Wang, *Coordin. Chem. Rev.*, 2016, 307,, 361-381.
23. Y. Jiao, J. Pei, C. Yan, D. Chen, Y. Hu and G. Chen, *J. Mater. Chem. A*, 2016, **4**, 13344-13351.
24. J. Yang, P. Xiong, C. Zheng, H. Qiu and M. Wei, *J. Mater. Chem. A*, 2014, **2**, 16640-16644.
25. J. Yang, Z. Ma, W. Gao and M. Wei, *Chem. Eur. J.*, 2017, **23**, 631 – 636.
26. L. Liu, Y. Yan, Z. Cai, S. Lin and X. Hu, *Adv. Mater. Interfaces*, 2018, **5**, 1701548.
27. Y. Zhou, Z. Mao, W. Wang, Z. Yang and X. Liu, *ACS Appl. Mater. Interface*, 2016, **8**, 28904-28916.

28. X. Xu, W. Shi, P. Li, S. Ye, C. Ye, H. Ye, T. Lu, A. Zheng, J. Zhu, L. Xu, M. Zhong and X. Cao, *Chem. Mater.*, 2017, **29**, 6058-6065.
29. P. Wen, P. Gong, J. Sun, J. Wang and S. Yang, *J. Mater. Chem. A*, 2015, **3**, 13874-13883.
30. Q. Wang, Q. Wang, B. Xu, F. Gao, F. Gao and C. Zhao, *Electrochim. Acta*, 2018, **281**, 69-77.
31. L. Shao, Q. Wang, Z. Ma, Z. Ji, X. Wang, D. Song, Y. Liu and N. Wang, *J. Power Sources*, 2018, **379**, 350-361.
32. Q. Wang, L. Shao, Z. Ma, J. Xu, Y. Li and C. Wang, *Electrochim. Acta*, 2018, **281**, 582-593.
33. Y. Jiao, G. Chen, D. Chen, J. Pei and Y. Hu, *J. Mater. Chem. A*, 2017, **5**, 23744-23752.
34. P. C. Banerjee, D. E. Lobo, R. Middag, W. K. Ng, M. E. Shaibani and M. Majumder, *ACS Appl. Mater. Interface*, 2015, **7**, 3655-3664.
35. Y. Zhong, X. Xia, F. Shi, J. Zhan, J. Tu and H. J. Fan, *Adv. Sci*., 2016, **3**, 1500286.
36. J. Zhou, J. Yu, L. Shi, Z. Wang, H. Liu, B. Yang, C. Li, C. Zhu and J. Xu, *Small*, 2018, **14**, 1803786.
37. M. R. Lukatskaya, O. Mashtalir, C. E. Ren, Y. Dall'Agnese, P. Rozier, P. L. Taberna, M. Naguib, P. Simon, M. W. Barsoum and Y. Gogotsi, *Science*, 2013, **341**, 1502-1505.
38. L. Yu, L. Hu, B. Anasori, Y. T. Liu, Q. Zhu, P. Zhang, Y. Gogotsi and B. Xu, *ACS Energy Lett*., 2018, **3**, 1597-1603.
39. R. Zhao, M. Wang, D. Zhao, H. Li, C. Wang and L. Yin, *ACS Energy Lett*., 2017, **3**, 132-140.
40. M. Boota, B. Anasori, C. Voigt, M. Q. Zhao, M. W. Barsoum and Y. Gogotsi, *Adv. Mater.*, 2016, **28**, 1517-1522.
41. R. Ramachandran, K. Rajavel, W. Xuan, D. Lin and F. Wang, *Ceram. Int*., 2018, **44**, 14425-14431.
42. L. Zhao, B. Dong, S. Li, L. Zhou, L. Lai, Z. Wang, S. Zhao, M. Han, K. Gao, M. Lu, X. Xie, B. Chen, Z. Liu, X. Wang, H. Zhang, H. Li, J. Liu, H. Zhang, X. Huang and W. Huang, *ACS Nano,* 2017, **11**, 5800-5807.
43. X. Wang, Q. Fu, J. Wen, M. Xinzhi, C. Zhu, X. Zhang and D. Qi, *Nanoscale*, 2018, **10**, 20828-20835.
44. S. Zhao, Y. Wang, J. Dong, C. T. He, H. Yin, P. An, K. Zhao, X. Zhang, C. Gao, L. Zhang, J. Lv, J. Wang, J. Zhang, A. M. Khattak, N. A. Khan, Z. Wei, J. Zhang, S. Liu, H. Zhao and Z. Tang, *Nat. Energy*, 2016, **1**, 16184.
45. Y. Wang, Y. Liu, H. Wang, W. Liu, Y. Li, J. Zhang, H. Hou, J. Yang, *ACS Appl. Energy Mater.*, 2019, **2**, 2063-2071.
46. W. Bao, D. Su, W. Zhang, X. Guo and G. Wang, *Adv. Funct. Mater.*, 2016, **26**, 8746-8756.
47. M. Naguib, M. Kurtoglu, V. Presser, J. Lu, J. Niu, M. Heon, L. Hultman, Y. Gogotsi and M. W. Barsoum, *Adv. Mater.*, 2011, **23**, 4248-4253.
48. Y. Wang, Y. Liu, H. Wang, W. Liu, Y. Li, J. Zhang, H. Hou and J. Yang, *ACS Appl. Energy Mater.*, 2019, **2**, 2063-2071.
49. J. Liu, T. Chen, P. Juan, W. Peng, Y. Li, F. Zhang and X. Fan, *Chem. Sus. Chem.*, 2018, **11**, 3758-3765.
50. S. Zhao, H. B. Zhang, J. Q. Luo, Q. W. Wang, B. Xu, S. Hong and Z. Z. Yu, *ACS Nano*, 2018, **12**, 11193-11202.
51. J. Jin, Y. Zheng, S.Z. Huang, P. P. Sun, N. Srikanth, L. B. Kong, Q. Yan and K. Zhou, *J. Mater. Chem. A*, 2019, **7**, 783 – 790.
52. Q. W. Wang, H. B. Zhang, J. Liu, S. Zhao, X. Xie, L. Liu, R. Yang, N. Koratkar and Z. Z. Yu, *Adv. Funct. Mater.*, 2018, **29**, 1806819.
53. Q. Xue, H. Zhang, M. Zhu, Z. Pei, H. Li, Z. Wang, Y. Huang, Y. Huang, Q. Deng, J. Zhou, S. Du, Q. Huang and C. Zhi, *Adv. Mater.*, 2017, **29**, 1604847.
54. P. Du, Y. Dong, C. Liu, W. Wei, D. Liu and P. Liu, *J. Colloid Interface Sci*., 2018, **518**, 57-68.
55. X. Liu, C. Shi, C. Zhai, M. Cheng, Q. Liu and G. Wang, *ACS Appl. Mater. Interface*, 2016, **8**, 4585-4591.
56. G. Zhu, H. Wen, M. Ma, W. Wang, L. Yang, L. Wang, X. Shi, X. Cheng, X. Sun and Y. Yao, *Chem. Commun*., 2018, **54**,10499-10502.
57. Q. Chen, S. Lei, P. Deng, X. Ou, L. Chen, W. Wang, Y. Xiao and B. Cheng, *J. Mater. Chem. A*, 2017, **5**, 19323-19332.
58. Q. Zhang, Z. Liu, B. Zhao, Y. Cheng, L. Zhang, H. H. Wu, M. S. Wang, S. Dai, K. Zhang, D. Ding, Y. Wu and M. Liu, *Energy Storage Mater.*, 2019, **16**, 632-645
59. W. Zhao, J. Peng, W. Wang, B. Jin, T. Chen, S. Liu, Q. Zhao and W. Huang, *Small*, 2019, **0**, 1901351.
60. X. Y. Liu, Y. Q. Zhang, X. H. Xia, S. J. Shi, Y. Lu, X. L. Wang, C. D. Gu and J. P. Tu, *J. Power Sources*, 2013, **239**, 157-163.
61. Q. Li, C. Lu, C. Chen, L. Xie, Y. Liu, Y. Li, Q. Kong and H. Wang, *Energy Storage Mater.*, 2017, **8**, 59-67.
62. J. Pu, F. Cui, S. Chu, T. Wang, E. Sheng and Z. Wang, *ACS Sustain. Chem. Eng.*, 2013, **2**, 809-815.
63. J. Fu, J. Yun, S. Wu, L. Li, L. Yu and K. H. Kim, *ACS Appl. Mater. Interfaces*, 2018, **10**, 34212-34221.
64. R. B. Rakhi, B. Ahmed, D. Anjum and H. N. Alshareef, *ACS Appl. Mater. Interfaces*, 2016, **8**, 18806-18814.
65. L. Kang, S. X. Sun, L. B. Kong, J. W. Lang and Y. C. Luo, *Chinese Chem. Lett.*, 2014, **25**, 957-961.